4*d* element induced improvement of structural disorder and development of weakly reentrant spin-glass behavior in NiRuMnSn

Shuvankar Gupta,[1,2,*] Sudip Chakraborty,[1,2] Vidha Bhasin,[3,2] Santanu Pakhira,[4] Anis Biswas,[4] Yaroslav Mudryk,[4] Amit Kumar,[5,2] Celine Barreteau,[6] Jean-Claude Crivello,[6] Amitabh Das,[5,2] S. N. Jha,[3] D. Bhattacharyya,[3] Vitalij K. Pecharsky,[4,7,†] Eric Alleno,[6] and Chandan Mazumdar[1,‡]

[1]*Condensed Matter Physics Division, Saha Institute of Nuclear Physics, 1/AF, Bidhannagar, Kolkata 700064, India*
[2]*Homi Bhabha National Institute, Anushaktinagar, Mumbai 400094, India*
[3]*Atomic & Molecular Physics Division, Bhabha Atomic Research Centre, Mumbai 400 094, Maharashtra, India*
[4]*Ames National Laboratory, Iowa State University, Ames, Iowa 50011, USA*
[5]*Solid State Physics Division, Bhabha Atomic Research Centre, Mumbai 400 085, India*
[6]*Univ. Paris Est Creteil, CNRS, ICMPE, UMR 7182, 2-8, rue H. Dunant, F-94320 Thiais, France*
[7]*Department of Materials Science and Engineering, Iowa State University, Ames, Iowa 50011, USA*

(Received 18 April 2023; revised 29 June 2023; accepted 14 July 2023; published 4 August 2023)

The pursuit of efficient spin polarization in quaternary Heusler alloys with the general formula $XX'YZ$ (where X, X', and Y are transition metals and Z is a p-block element) has been a subject of significant scientific interest. While previous studies showed that isoelectronic substitution of a 4*d* element in place of a 3*d* element in quaternary Heusler alloys improves the half-metallic ferromagnetic characteristics, our research on the quaternary Heusler alloy NiRuMnSn reveals a strikingly different scenario. In this study, we present a detailed structural analysis of the material using x-ray absorption fine structure and neutron diffraction techniques which confirms the formation of a single-phase compound with 50:50 site disorder between Ni and Ru atoms at 4*c* and 4*d* sites. Contrary to expectations, our density functional theory calculations suggest a considerable decrease in spin polarization even in the ordered structure. Additionally, we report on the compound's exceptional behavior, displaying a rare reentrant spin-glass property below ∼60 K, a unique and intriguing feature for quaternary Heusler-type compounds.

DOI: 10.1103/PhysRevB.108.054405

I. INTRODUCTION

The extended family of so-called Heusler alloys continues to attract considerable attention from the condensed matter physics and materials science communities due to the plethora of tailorable properties that are both fundamentally interesting and potentially functional. Well-known examples include half-metallic ferromagnetism (HMF) [1], ferromagnetic shape memory effects [2], the formation of magnetic skyrmions [3], topological phenomena and Weyl semimetallicity [4], unusual thermoelectricity [5,6], and the giant magnetocaloric effect [7]. Generally, Heusler phases are classified as either full Heusler, commonly represented by the idealized X_2YZ stoichiometries, where X and Y are transition elements and Z is a main-group element, or half Heusler, often denoted as XYZ compounds [8]. Structurally ordered full Heusler alloys crystallize with the $L2_1$-type structure (space group: $Fm\bar{3}m$, No. 225) that consists of four interpenetrating fcc lattices. For the case of half Heusler alloys, one of the fcc lattice sites remains vacant, and it crystalizes in the Y type of crystal structure (space group: $F\bar{4}3m$, No. 216) [8]. A rather simple cubic crystal structure makes them an ideal model system for basic research focused on the fundamental understanding of d-band magnetism [9–12]. Apart from this, the half-metallic properties of many Heusler alloys are useful in the field of spintronics [13], which makes use of high spin polarization due to the unique band structures of HMF Heusler alloys, in which one spin channel is metallic and the other spin channel is semiconducting in nature [14].

It is generally found that the degree of spin polarization in HMF systems is very sensitive to structural disorder [15–18]. As materials that belong to the Heusler family often include elements from the same period of the periodic table (e.g., 3*d* elements), they crystallize in disordered structures, making it challenging to synthesize Heusler phases with negligible site disorder. In order to tune the Fermi energy E_F in the middle of the gap, which makes the HMF property more robust against external perturbation, partial substitutions at the Y site in full Heusler systems are often found to be effective. However, such substitution often results in considerable structural disorder, which, in turn, reduces spin polarization [19]. On the other hand, replacing half of the X atoms by another transition element, X', is possible, leading to quaternary Heusler alloys ($XX'YZ$) [20]. The latter crystalize in the Y-type (LiMgPdSn-type) structure (space group: $F\bar{4}3m$, No. 216), in which each of the four interpenetrating lattices is occupied by four different elements [19], which is achieved by splitting the 8*c*

*guptashuvankar5@gmail.com
†Deceased.
‡chandan.mazumdar@saha.in

site in $Fm\bar{3}m$ into the 4*c* and 4*d* sites in $F\bar{4}3m$. Research on quaternary Heusler alloy systems has mainly focused on 3*d*-based transition elements [21–27], whereas only a handful of 4*d*-based (Ru, Rh) Heusler alloys have been reported in the literature [28,29]. The 4*d*-based Heusler alloys are known to form with negligibly small structural disorder, and thus, they show enhanced magnetic ordering temperatures without altering the basic nature of the magnetic characteristics of their 3*d*-based counterparts [29]. For example, CoFeMnGe crystallizes in the $D0_3$-type disordered structure (3*d* elements are statistically distributed among three different sites) due to the presence of elements of nearly equal size [30]. However, when Fe is replaced by Rh, the compound CoRhMnGe crystallizes in the *Y*-type ordered structure [28].

NiFeMnSn is a 3*d*-based quaternary Heusler phase that exhibits a moderately high Curie temperature, $T_C \sim 405$ K, which is theoretically claimed to possess a moderately high spin polarization of ∼70% in the ordered structure [17,18]. However, due to the presence of inherent structural disorder in the experimentally synthesized compound, the half metallicity is considerably diminished, and the compound becomes metallic. An isoelectronic substitution of the 4*d* element Ru in place of the 3*d* element Fe is expected to enhance the spin polarization through improved structural ordering. Through our detailed experimental and theoretical investigation, we, however, find that despite achieving a much improved atomic periodicity in NiRuMnSn, spin polarization actually deteriorates, which we have assigned to the much weaker magnetic character of Ru compared to Fe. This nonmagnetic (or weakly magnetic) character of Ru also results in the appearance of weakly reentrant spin-glass behavior, which is very rare in the equiatomic quaternary Heusler alloy family.

II. METHODS

A. Experiment

The polycrystalline NiRuMnSn was prepared by arc melting a stoichiometric mixture of high-purity (>99.99%) constituent elements in a flowing argon environment. To compensate for the losses due to the vaporization of Mn, the element was weighed with 2 wt % excess. To improve homogeneity, the alloy was remelted five times; the button was flipped after each melt. The x-ray diffraction (XRD) analysis of the powdered sample at room temperature was performed with Cu $K\alpha$ radiation using a rotating anode TTRAX-III diffractometer (Rigaku Corp., Japan). The sample's phase purity and crystal structure were determined by performing Rietveld refinement using the FULLPROF software package [31]. Dc magnetization measurements were carried out in a commercial superconducting quantum interference device (SQUID) magnetometer (Quantum Design, United States) at temperatures of 5–380 K under applied magnetic fields of $-70 \leqslant H \leqslant 70$ kOe. Ac magnetic susceptibility measurements were performed in an MPMS XL-7 SQUID magnetometer (Quantum Design). Electrical resistivity was measured with a four-probe technique using a physical property measurement system (Quantum Design). The extended x-ray absorption fine structure (EXAFS) measurements were performed at the BL-9 beamline at the Indus-2 Synchrotron Source (2.5 GeV, 100 mA) at the Raja Ramanna Centre for Advanced Technology, Indore, India [32,33]. For the studied compound, EXAFS measurements were performed on the Ni, Ru, and Mn *K* edges in the energy range of 4–25 keV.

The collimating meridional cylindrical mirror is covered with Rh/Pt, and the collimated beam reflected by the mirror is monochromatized by a Si(111) ($2d = 6.2709$ Å) based double crystal monochromator (DCM). The second DCM is a sagittal cylinder that is utilized for horizontal focusing, and a Rh/Pt-coated bendable post mirror facing down is used for vertical focusing at the sample position. Detuning the second crystal of the DCM is used to reject the higher harmonic content in the x-ray beam. EXAFS measurements in both transmission and fluorescence modes are possible in this beamline. For this case, the measurements were done in the fluorescence mode, with the sample at 45° to the incident x-ray beam and a fluorescence detector at right angles to the incident x-ray beam to capture the signal. The incident flux I_0 is measured by one ionization chamber detector, and the fluorescence intensity I_f is measured by a florescence detector. The spectra were acquired as a function of energy by scanning the monochromator across the prescribed range, and the absorption coefficient μ was obtained using the relation $I_f = I_0 e^{-\mu x}$, where x is the thickness of the absorber. Oscillations in the absorption spectra [$\mu(E)$ vs E] have been translated to the EXAFS function $\chi(E)$ defined as [34]

$$\chi(E) = \frac{\mu(E) - \mu_0(E)}{\Delta\mu_0(E_0)}, \tag{1}$$

where E_0 is the absorption edge energy, $\mu_0(E_0)$ is the bare atom background, and $\Delta\mu_0(E_0)$ is the absorption edge step in the $\mu(E)$ value. $\chi(E)$ has been transformed to the wave number dependent absorption coefficient $\chi(k)$ using the relation

$$k = \sqrt{\frac{2m(E - E_0)}{\hbar^2}}, \tag{2}$$

where m is the electron mass, $\chi(k)$ is weighted by k^2 to amplify the oscillation at high k, and the $\chi(k)k^2$ functions are Fourier converted in R space to obtain the $\chi(R)$ vs R graphs in terms of distance in real space (phase uncorrected) from the center of the absorbing atom. For EXAFS data analysis, a suite of EXAFS data analysis programs included in the DEMETER software package [35] was employed. This includes background reduction and Fourier transform to derive the $\chi(R)$ vs R plots from absorption spectra (using the ATHENA code), the generation of theoretical EXAFS spectra based on an assumed crystallographic structure, and, finally, fitting experimental data to theoretical spectra using the ARTEMIS code. Powder neutron diffraction data were recorded on the PD2 powder neutron diffractometer ($\lambda = 1.2443$ Å) at the Dhruva reactor, Bhabha Atomic Research Centre, Mumbai, India. Neutron depolarization measurements were performed on the polarized neutron spectrometer at the Dhruva reactor.

B. Computational

The structural stability and ground-state properties of the system are theoretically investigated using the density functional theory (DFT). DFT calculations were conducted using

the projector augmented wave method [36] implemented in the Vienna Ab initio Simulation Package (VASP) [37,38]. The exchange correlation was described by the generalized gradient approximation modified by Perdew, Burke, and Ernzerhof [39]. Energy bands up to a cutoff energy, $E_{\text{cutoff}} = 600$ eV, were included in all calculations. After volume and ionic (for disordered compounds) relaxation steps were performed, the tetrahedron method with Blöchl correction [40] was applied. For all cases, the spin-polarization calculations were appropriately considered. In order to model disorder in NiRuMnSn, unit cells based on the concept of special quasirandom structure (SQS) [41] were generated to model different possible disorder schemes. To generate the SQS, the cluster expansion formalism for multicomponent and multisublattice systems [42] was used as implemented in the Monte Carlo code (MCSQS) contained in the Alloy-Theoretic Automated Toolkit (ATAT) [43,44]. Subsequent DFT calculations were performed in order to test the quality of the SQS and to determine the reliability of the DFT results. The rms error was used as another quality criterion in addition to the calculations including a different order of interactions. The rms error describes the deviation of the correlation function of the SQS Π^k_{SQS} from the correlation functions of considered clusters k for a given random structure Π^k_{md},

$$\text{rms} = \sqrt{\sum_k \left(\Pi^k_{\text{SQS}} - \Pi^k_{\text{md}}\right)^2}. \tag{3}$$

Several tests for the dependence of the cluster type and nearest-neighbor numbers were done to generate the disordered structure with Sn in 4*a* (0,0,0), Mn in 4*b* (0.5,0.5,0.5), 0.5Ru + 0.5Ni in 4*c* (0.25,0.25,0.25), and 0.5Ru + 0.5Ni in 4*d* (0.75,0.75,0.75). Finally, 7 first-pair, 5 triplet, and 11 quadruplet interactions were considered to obtain reliable results. For the 4*c*/4*d*-disordered *Y* phase, a quaternary SQS cell of 28 atoms was built.

III. RESULTS AND DISCUSSION

A. Structure optimization and electronic structure calculations

DFT calculations on NiRuMnSn using different atomic arrangements within the LiMgPdSn-type structure were first performed to find the most stable configuration. In a quaternary Heusler alloy $XX'YZ$, assuming Z element atoms occupy the 4*a* (0,0,0) site, the three remaining elements, X, X', and Y, can be placed on 4*b* (0.5, 0.5, 0.5), 4*c* (0.25, 0.25, 0.25), and 4*d* (0.75, 0.75, 0.75) sites. Further, considering that switching atoms between the 4*c* and 4*d* sites results in energetically degenerate configurations, out of six total possible ordered NiRuMnSn structures, only the three that are listed in Table I and depicted in Fig. 1 are distinguishable.

TABLE I. Calculated enthalpy of formation $\Delta_f H$ for three different ordered types and one disordered structural atomic arrangement of NiRuMnSn.

	4*a*	4*b*	4*c*	4*d*	$\Delta_f H$ (kJ/mol)
Type 1	Sn	Mn	Ni	Ru	−8.19
Type 2	Sn	Ru	Mn	Ni	14.80
Type 3	Sn	Ni	Ru	Mn	8.95
Disordered	Sn	Mn	Ni:Ru	Ni:Ru	−11.14

The DFT-calculated enthalpies of formation presented in Table I show that the ordered type-1 structure (with Ni and Ru in the same planes) is more stable than type-2 and type-3 structures, which is consistent with site preferences in other quaternary Heusler compounds, where the least electronegative atoms occupy the 4*b* site. Figure 2 shows the calculated density of states (DOS) of the energetically most favorable type-1 ordered and disordered structures (discussed later). We note that the DOS reveals no band gaps in either for spin-up or spin-down states. Additionally, the calculated spin polarization (44.6%) is moderate, and the calculated total magnetic moment, 4.3 μ_B (Ni = 0.46 μ_B, Ru = 0.31 μ_B, and Mn = 3.53 μ_B), is close to the value of 5 μ_B predicted by the Slater-Pauling rule [45,46]. The electronic structures of the compounds, whether they belong to ordered or disordered crystal structures, are quite similar. The interaction of *sp* Sn states with the other *d* elements causes the first bands to form between −10 and −8 eV below the Fermi level. The major structure is then dominated by a combination of Mn, Ni, and Ru 3*d* and 4*d* bands starting at −6.5 eV. The Ni and Ru states are almost filled, which accounts for the weak ferromagnetic behavior of the material, although Mn still has some electronic

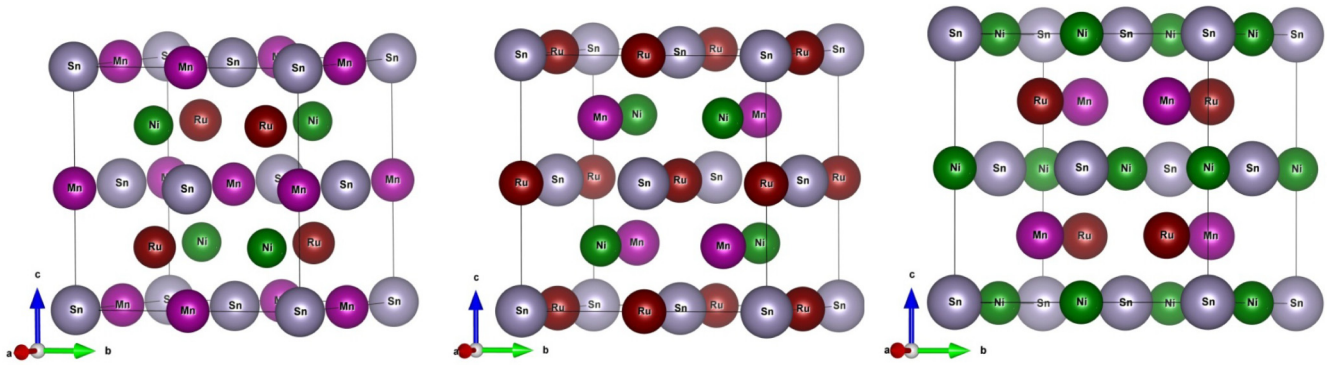

(a) Type 1 (b) Type 2 (c) Type 3

FIG. 1. Unit cell representation of (a) type-1, (b) type-2, and (c) type-3 ordered structures as described in Table I. Sn, Mn, Ni, and Ru atoms are represented by gray, magenta, green, and red balls, respectively.

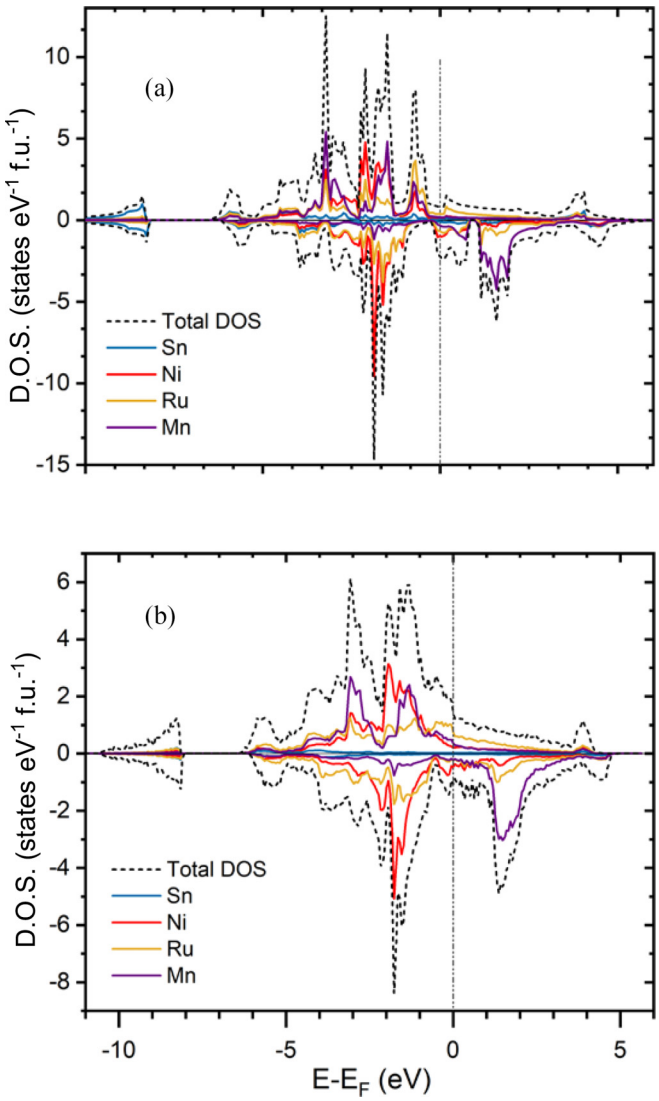

FIG. 2. Atom-resolved density of states for (a) the ordered structure and (b) the disordered structure.

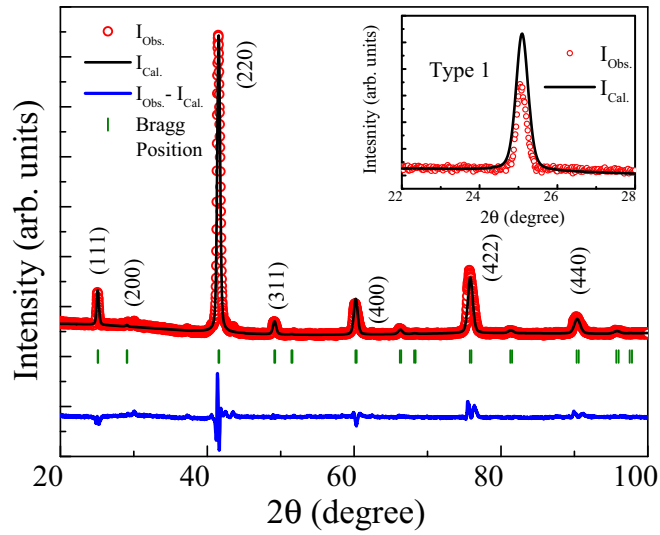

FIG. 3. Rietveld refinement of the powder XRD pattern of NiRuMnSn (assuming disordered structure) measured at room temperature. The inset highlights the Rietveld refinement results using the (111) peak as an example when considering the ordered structure (type 1).

holes. The Ni/Ru mixed structure displays a smoother variation of the DOS with fewer peaks of high density compared to the ordered structure, which displays relatively flat bands and therefore sparse and intense peaks in the DOS.

B. X-ray diffraction

Theory predicts (Table I) that the type-1 structure, in which Sn occupies the 4*a* position, Mn occupies 4*b*, Ru occupies 4*d*, and Ni occupies 4*c* positions, has lower energy compared to the other two types of ordered structures. In other words, the most stable ordered structure should consist of Sn/Mn and Ni/Ru layers. However, the Rietveld refinement of the powder XRD pattern taken at room temperature does not support the formation of the fully ordered type-1 structure because the intensity of the (111) peak, as illustrated in the inset of Fig. 3, cannot be described satisfactorily using the atomic positions from Table I. Since intensities of both the (111) and (200) Bragg peaks are most indicative of the presence of structural disorder, the mismatch between the observed and calculated intensities of the (111) peak suggests the presence of structural disorder in the type-1 arrangement of the crystal lattice [19,25,47]. Out of the different types of disorder present in Heusler alloys, the *A*2 (space group: $Im\bar{3}m$, No. 229) and *B*2 (space group: $Pm\bar{3}m$, No. 221) types are known to occur most frequently. For the *A*2-type structure, both the (111) and (200) peaks are absent, whereas only the (200) peak is present in the *B*2-type [8,19,25]. In the *A*2-type structure, all the constituent atoms (X, X', Y, and Z) randomly mix with each other, while for the *B*2 type, the Y and Z and X and X' atoms randomly mix with each other in the 4*b* and 4*a* and 4*c* and 4*d* sites, respectively. The clear presence of the (111) peak and near absence of the (200) Bragg peak therefore contradict both the *A*2- and *B*2-type disorders in the title material.

A model in which Ni and Ru atoms mix with each other in the 4*c* and 4*d* positions, on the other hand, leads to a satisfactory fit of intensities of all Bragg peaks present in the powder diffraction pattern (Fig. 3). This disorder between the Ni and Ru atoms transforms the *Y*-type ordered structure (space group: $F\bar{4}3m$, No. 216) into a variant of the $L2_1$-type (space group: $Fm\bar{3}m$) structure typical of ordered ternary Heusler compounds. The disordered crystal structure is presented in Fig. 4. Subsequently, we also checked the ground-state energy for this disordered structure and found it has lower formation enthalpy (−11.14 kJ/mol) compared to the ordered type-1 structure (see Table I), consistent with experimental results. A similar type of disorder in Co and Ru atoms was previously reported for CoRuMnSi [48]. The lattice parameter determined by Rietveld refinement is $a = 6.145(4)$ Å.

C. Extended x-ray absorption fine structure

Details of the crystal structure may be difficult to establish conclusively using x-ray powder diffraction alone, particularly when two elements with similar atomic scattering

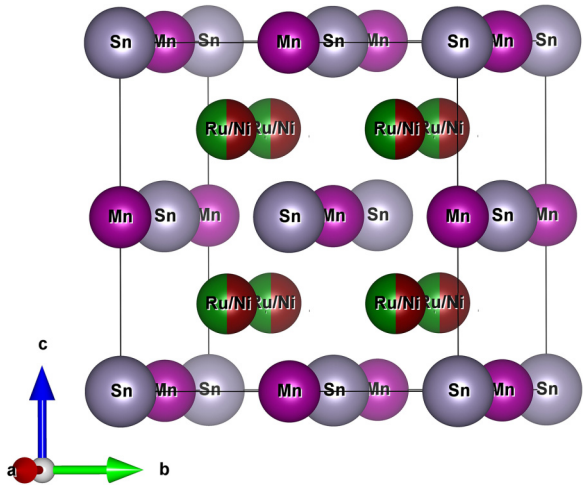

FIG. 4. Atomic arrangement in the disordered crystal structure of NiRuMnSn.

factors, in this case Mn and Ni, are present in the same lattice. Other experiments, such as EXAFS and neutron diffraction (ND) [17,49–51], are therefore highly beneficial for determining the exact atomic arrangements in the title system. In contrast to XRD, EXAFS is an element-specific measurement that focuses on the local atomic environment around the absorbing atoms. Therefore, to better understand the nature of disorder, we performed the EXAFS measurements at the Ni, Ru, and Mn K edges. Figure 5 shows the normalized EXAFS [$\mu(E)$ vs E] spectra of NiRuMnSn at the Ni, Ru, and Mn K edges.

Figure 6 shows the Fourier transformed EXAFS spectra [$\chi(R)$ vs R] plots of the Ni, Ru, and Mn edges for NiRuMnSn. Simultaneous fitting of various data sets with numerous edges is the fitting approach used here [51]. The $\chi(R)$ vs R plots measured at the Ni, Ru, and Mn edges are fitted simultaneously with common fitting parameters. The number of independent parameters is reduced below the Nyquist requirements, and the statistical significance of the fitted model is improved. The goodness of the fit determined by the value of R_{factor} is described by

$$R_{\text{factor}} = \frac{\{\text{Im}[\chi_{\text{dat}}(r_i)-\chi_{\text{th}}(r_i)]\}^2 + \{\text{Re}[\chi_{\text{dat}}(r_i)-\chi_{\text{th}}(r_i)]\}^2}{\{\text{Im}[\chi_{\text{dat}}(r_i)]\}^2 + \{\text{Re}[\chi_{\text{dat}}(r_i)]\}^2}, \tag{4}$$

where χ_{dat} and χ_{th} are the experimental and theoretical $\chi(R)$ values and Im and Re are the imaginary and real components of the related quantities, respectively. For theoretical simulation of the EXAFS spectra of NiRuMnSn, the structural parameters were obtained from the XRD results. Bond distances R, coordination numbers N, and disorder (Debye-Waller) factors σ^2, which give the mean-square variations in the distances, were employed as fitting parameters during the fitting process. The fitting was done up to 2.8 Å for Ni- and Ru-edge data and up to 3.8 Å for Mn-edge data.

The EXAFS fitted results are summarized in Table II. In the Fourier transformed EXAFS spectrum of the Ni K edge [Fig. 6(a)], the main peak near 2 Å has contributions from the Ni-Mn (2.63 Å) and Ni-Sn (2.63 Å) paths. The small

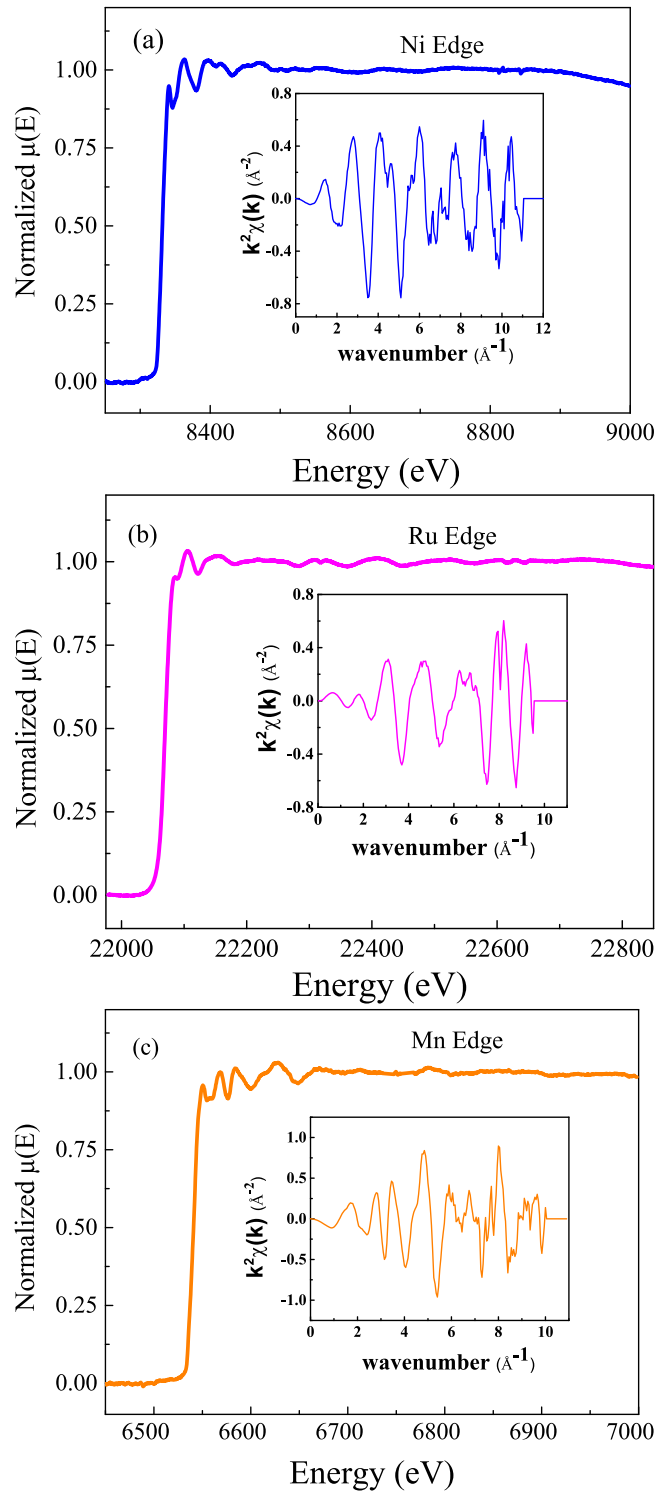

FIG. 5. Normalized EXAFS spectra of NiRuMnSn taken at (a) the Ni edge, (b) the Ru edge, and (c) the Mn edge. The insets show the EXAFS signal $\chi(k)$, weighted by k^2, plotted as a function of k.

peak around 2.5 Å in the Ni-edge spectrum includes contributions from the Ni-Ni (3.00 Å) and Ni-Ru (3.00 Å) paths. For the case of the Ru K edge, of two main peaks observed in the Fourier transformed (FT) EXAFS spectrum [Fig. 6(b)], the first peak near 2 Å has contributions from the Ru-Mn

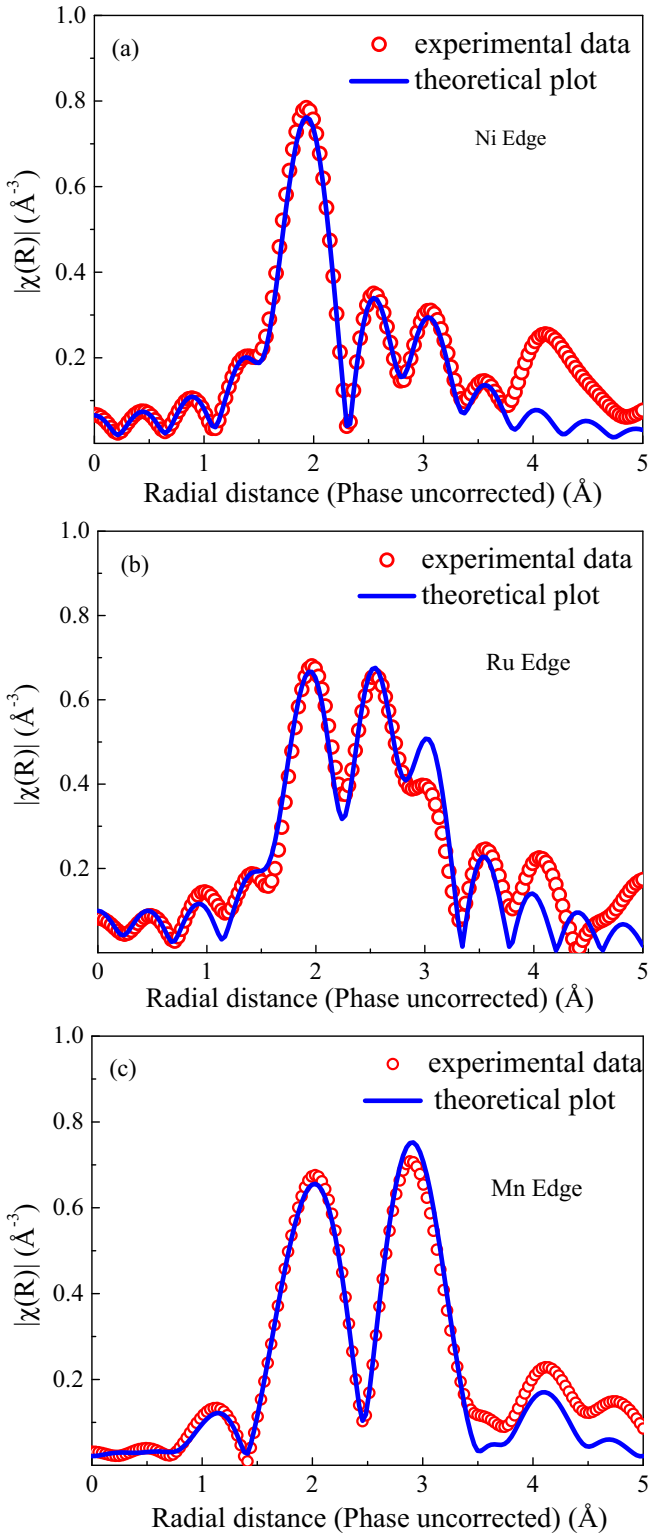

FIG. 6. Fourier transformed EXAFS spectra of NiRuMnSn taken at (a) the Ni edge, (b) the Ru edge, and (c) the Mn edge (red points) and the theoretical fit (solid blue lines).

(2.57 Å) and Ru-Sn (2.57 Å) paths, whereas the second peak observed at 2.5 Å has contributions from the Ru-Ni (3.00 Å) and Ru-Ru (3.00 Å) paths. In a similar way, for the case of Mn K edge, the first major peak near 2 Å in the FT-EXAFS spectrum [Fig. 6(c)] has contributions from the Mn-Ni (2.62 Å) and Mn-Ru (2.60Å) paths. The second peak in the Mn FT-EXAFS spectrum near 2.8 Å has contributions from the Mn-Sn (3.06 Å) and Mn-Mn (4.32 Å) paths. Earlier x-ray diffraction results suggested a 50:50 swap disorder between the Ni and Ru atoms. It is worth mentioning here that simultaneous fitting of all the edges (Ni, Ru, and Mn) in the EXAFS data would be possible only assuming disordered structure. It should be noted that, generally, we do not vary the coordination number or number of neighbors N during the EXAFS fitting, and hence, no error bars have been attributed to these values in Table II. However, the x-ray diffraction results for the sample indicate the presence of swap disorder between Ni and Ru atoms. Hence, we have considered a relative Ni/Ru atomic weightage factor in the case of Ni-Ni and Ni-Ru coordination shells for Ni-edge data, Ru-Ni and Ru-Ru coordination shells in the case of Ru-edge data, and Mn-Ni and Mn-Ru coordination shells in the case of Mn-edge data. These atomic weightage factors were varied during fitting of the EXAFS data of the respective edges, and the final coordination numbers obtained for these coordination shells are given in Table II. Our EXAFS analysis thus obtained is found to be quite consistent with x-ray diffraction (Sec. III B) and DFT calculations results (Table I).

D. Magnetic properties

Figure 7 represents the magnetization M vs temperature T of NiRuMnSn measured during zero-field-cooled (ZFC) heating and field-cooled (FC) cooling in a 100 Oe magnetic field. The compound undergoes broad ferromagnetic $\longleftrightarrow$ paramagnetic transition at the Curie temperature T_C centered near 214 K as determined from the minima of $d(M/H)/dT$. ZFC and FC data bifurcate below T_C, and the ZFC curve shows a peak at T_P around 60 K, below which magnetization begins to decrease with decreasing temperature. In the case of the FC measurement, magnetization below T_P is substantially enhanced compared to ZFC data, and the peak becomes nearly indistinguishable. T_P shifts towards lower temperatures with the application of higher magnetic fields, as shown in the inset of Fig. 7. This type of behavior is frequently observed in cases of antiferromagnetic (AFM) or spin-glass-type states at low temperatures [12,52–54]. Based upon on the magnetization data, three possible scenario can be envisaged: (i) Spin reorientation or canting of the existing ferromagnetic arrangement occurs. (ii) Because of structural disorder, only a fraction of the phase orders ferromagnetically at $T_C \sim 214$ K, while the rest exhibits the magnetic transition at T_P. (iii) Magnetic inhomogeneity develops within a ferromagnetically ordered phase, where multiple magnetic phases coexist below T_P. Additionally, a downward bending of the (H/M) curve above T_C is clearly observed. This behavior suggests the presence of short-range order above T_C; that is, the material consists of regions or domains with enhanced magnetic susceptibility. These regions are likely to interact with each other, leading to the observed downward bending in inverse magnetic susceptibility above T_C. The positive value of θ_{CW} (∼219 K), which is close to T_C (∼214 K), indicates the dominating nature of ferromagnetic (FM) interactions in our sample. As the magnetic susceptibility alone cannot distinguish between the above three possibilities, we carried out isothermal

TABLE II. Bond length R, coordination number N, and Debye-Waller or disorder factor σ^2 obtained by EXAFS fitting for NiRuMnSn at the Ni, Ru, and Mn edges.

Ni edge				Ru edge				Mn edge			
Path	R (Å)	N	σ^2	Path	R (Å)	N	σ^2	Path	R (Å)	N	σ^2
Ni-Mn	2.63±0.01	4	0.0106 ±0.0017	Ru-Mn	2.57±0.01	4	0.0210±0.0048	Mn-Ni	2.62±0.03	5.4	0.0161±0.0041
Ni-Sn	2.63±0.01	4	0.0093±0.0014	Ru-Sn	2.57±0.01	4	0.0095±0.0030	Mn-Ru	2.60±0.03	2.6	0.0057±0.0030
Ni-Ni	3.00±0.03	1.7	0.0168±0.0048	Ru-Ni	3.00±0.03	3.5	0.0069±0.0011	Mn-Sn	3.06±0.02	6	0.0115±0.0020
Ni-Ru	3.00±0.03	4.3	0.0135±0.0048	Ru-Ru	3.00±0.03	2.5	0.0018±0.0007	Mn-Mn	4.32±0.05	12	0.0282±0.0081

magnetization, neutron diffraction, neutron depolarization, and ac susceptibility measurements for clarity.

Figure 8(a) illustrates the isothermal magnetization $M(H)$ of the title material measured at 3 K after zero-field cooling. Despite a ferromagnetic like character, $M(H)$ remains far from saturation even at 70 kOe, apparently being a superposition of (dominant) soft ferromagnetic and (weaker) linear contributions, indicating the presence of an AFM or paramagnetic phase in addition to the FM phase [Fig. 8(a)]. Moreover, the magnetic moment under application of 70 kOe at 3 K is found to be of 2.17 μ_B/f.u., which appears to be considerably smaller in comparison to the value of 5μ_B/f.u. expected from the Slater-Pauling (SP) rule [45,46]. The spontaneous magnetization, which is defined as the net magnetization of the system in the absence of external magnetic field, is estimated from the linear extrapolation of saturation magnetization to $H = 0$ Oe and found to be 1.77 μ_B/f.u. [inset of Fig. 8(a)]. The Curie-Weiss fit of the H/M versus T data measured at a 100 Oe magnetic field in the temperature regime of 320–380 K yields an effective paramagnetic moment of 3.93 μ_B/f.u., which is, coincidentally, close to the value predicted by the DFT calculation (4.3 μ_B, Sec. III A). It should be noted that the magnetic moment obtained from neutron diffraction study (1.69 μ_B/f.u., Sec. III E) agrees quite well with the spontaneous magnetization (1.77 μ_B/f.u., this section) at low temperature. Comparing NiRuMnSn and NiFeMnSn, it is clear that the introduction of the 4*d* element Ru dramatically alters the magnetic properties of the purely 3*d* element based NiFeMnSn [17]. Thus, the Curie temperature is reduced from 405 K in NiFeMnSn to 214 K in NiRuMnSn, and the saturation magnetization at low temperatures is suppressed from 4.18 μ_B/f.u. in NiFeMnSn to 2.17 μ_B/f.u. in NiRuMnSn. This is quite unusual because in most of the known Heusler alloys (e.g., CoFeMnSi [23], CoRhMnGe [28], CoFeMnGe [30], and CoRuMnSi [48]), the substitutions of Fe with Ru or Rh do not affect the magnetism

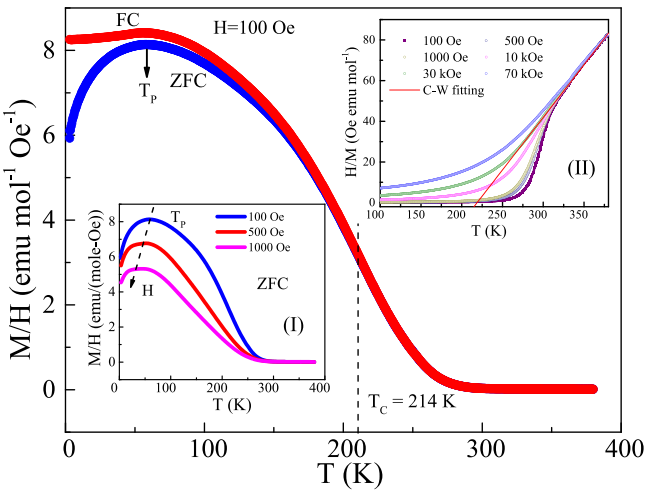

FIG. 7. Temperature dependence of the magnetization of NiRuMnSn measured under a 100 Oe applied magnetic field under ZFC and FC configurations. Inset I shows ZFC magnetization at different fields, demonstrating the shift of peak temperature T_P with the application of field, and inset II shows the H/M versus T plot for different applied magnetic fields and the Curie-Weiss fit.

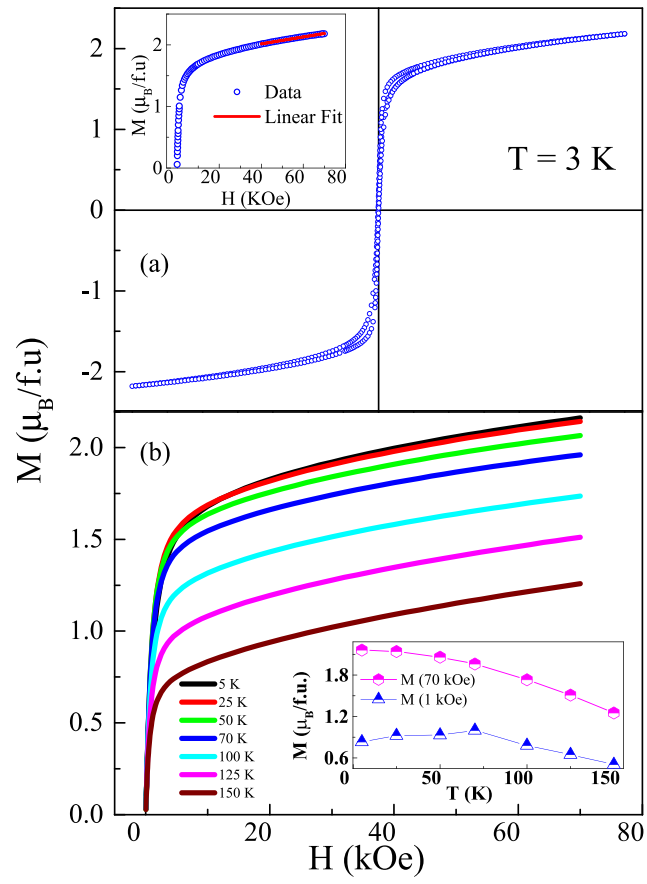

FIG. 8. (a) Isothermal magnetization $M(H)$ of NiRuMnSn measured at 3 K. The inset shows linear fitting of the high field data. (b) Single quadrant $M(H)$ taken at different temperatures; the inset shows the temperature dependence of the scatter plot of the magnetization at 1 and 70 kOe.

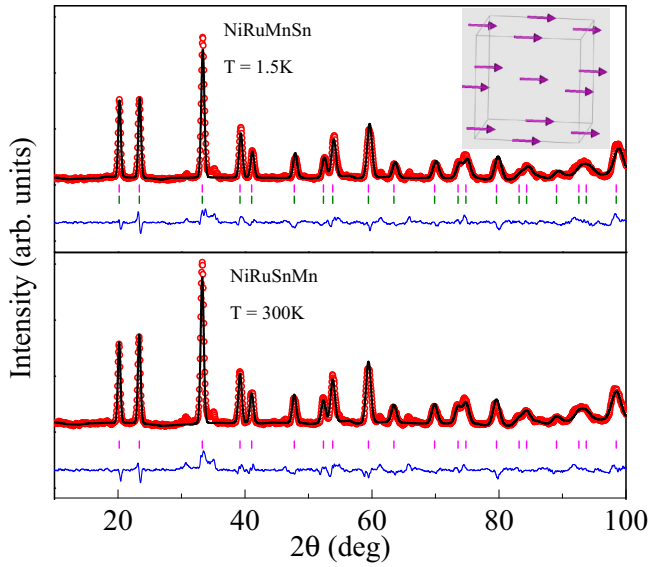

FIG. 9. Rietveld refinement of the neutron diffraction pattern of NiRuMnSn taken at 1.5 and 300 K. The inset depicts the magnetic structure of NiRuMnSn, where spins are developed on the Mn atom.

in such a drastic way, and importantly, compounds containing Co in the X site closely obey the SP rule. Interestingly, a closer investigation of the magnetic isotherms [Fig. 8(b)] reveals the magnetization at low field values mimics the anomaly [inset of Fig. 8(b)] observed in M/H versus T data (Fig. 7), whereas the high field (70 kOe) value follows a mean-field-like behavior, which is commonly observed for ferromagnetic systems. For a purely ferromagnetic system, such an anomaly in the low field region is not expected and thus suggests that the contribution of the ferromagnetic phase gets weakened due to the disturbance of the ferromagnetic spin structure by spin canting or reorientation or the development of spin-/cluster-glass behavior. Since neutron diffraction measurements can detect the change in magnetic spin structure, we carried them out at different temperatures in the range 1.5–300 K.

E. Neutron diffraction and neutron depolarization

Neutron diffraction measurement not only is helpful for understanding the magnetic structure but can also be utilized as a tool complementary to XRD for detailed structural characterization of a system, particularly when multiple atoms with similar atomic numbers are involved. The scattering lengths of Ni, Ru, Mn, and Sn are 1.030×10^{-12}, 0.7030×10^{-12}, -0.3730×10^{-12}, and 0.6225×10^{-12} cm, respectively, making it possible to confirm the site occupancies previously postulated from the analysis of the x-ray diffraction data. Figure 9 shows the Rietveld-refined neutron diffraction patterns recorded at 300 and 1.5 K. The data at 300 K are fitted in the $Fm\bar{3}m$ space group with atoms occupying the following positions: Sn in 4a (0,0,0), Mn in 4b (0.5, 0.5, 0.5) with full occupancy, and Ni/Ru in 4c (0.25, 0.25, 0.25) and 4d (0.75, 0.75, 0.75) with 50:50 occupancy. A fully random distribution of Ni and Ru between 4c and 4d sites yields the best fit, in agreement with the analysis of XRD and EXAFS data.

At 1.5 K, weak enhancements of the intensities of (111) and (200) reflections are observed (Fig. 9). The absence of additional reflections rules out the presence of long-range AFM ordering. The enhanced intensities of the fundamental reflections at 1.5 K indicate a FM arrangement of the magnetic moments, which was modeled assuming Mn is the only magnetic species (consistent with DFT calculations in Sec. III A) in F-1 space group. The refined total magnetic moment of Mn at 1.5 K is 1.69 μ_B/f.u., which is consistent, within error, with the 1.77 μ_B/f.u. spontaneous magnetic moment estimated from the isothermal magnetization measurements at 3 K [inset of Fig. 8(a)]. An analysis of ND data could not detect any moment on the Ni site, suggesting the Ni moment, if any, in this compound is below the limit of resolution of the experiment. This is expected because the Ni and Ru atoms at the 4c and 4d sites are randomly distributed, which strongly hinders the possibility of long-range ordering of the Ni spins. The absence of any change in magnetic structure before and after T_P excludes the possibility of any spin canting/reorientation in the system. Thus, the anomaly in the magnetic susceptibility at T_P can be attributed to only the development of a spin-/cluster-glass phase. Combining the observation of lower magnetic moment in the low field region for $T < T_P$ and the conservation of the ferromagnetic spin structure at the lowest temperature suggested by the neutron diffraction measurement, the reduction in $M(T)$ in both the ZFC and FC configurations is likely due to the development of a glassy phase at the partial expense of ferromagnetically ordered spins.

A neutron depolarization experiment is a very effective tool to study the growth and development of ferromagnetic domains. Accordingly, we carried out the neutron depolarization measurement in the temperature range of 2–300 K, covering both T_C and T_P. In a neutron depolarization experiment, the polarization vector of a polarized neutron beam is examined after the beam passes through a magnetic medium. As the magnetic inhomogeneities in the medium influence the polarization vector during transmission, the mean magnetic induction causes a net rotation of the polarization vector. In the presence of spontaneous magnetization, the local magnetic induction results in an effective rotation of the polarization vector, which is known as depolarization. This characteristic can be used to distinguish a purely ferromagnetic system from any other kind of magnetic ordering. The frequency of spin fluctuations in the paramagnetic state is too high for neutron polarization to be affected, and no depolarization is observed [55,56]. In a spin-glass system, as the spins are frozen randomly, the random spatial fluctuations of the effective field cannot influence the polarization vector either. Depolarization is also not expected in AFM materials since net magnetization is zero. In contrast, in ferromagnets, the neutron spins experience torque around the magnetization axes as they travel through equally magnetized domains, resulting in the loss of polarization [52,57,58]. Thus, by using a neutron depolarization experiment, one can estimate the mean orientation of these fluctuations (magnetic texture), the mean magnetization, and the magnetic correlation length along the neutron route.

For the present NiRuMnSn sample, neutron depolarization is measured in the temperature range of 5–300 K in the presence of a magnetic field of 50 Oe in the ZFC mode (Fig. 10). As the temperature is lowered from room temperature, the polarization does not exhibit any significant changes in the

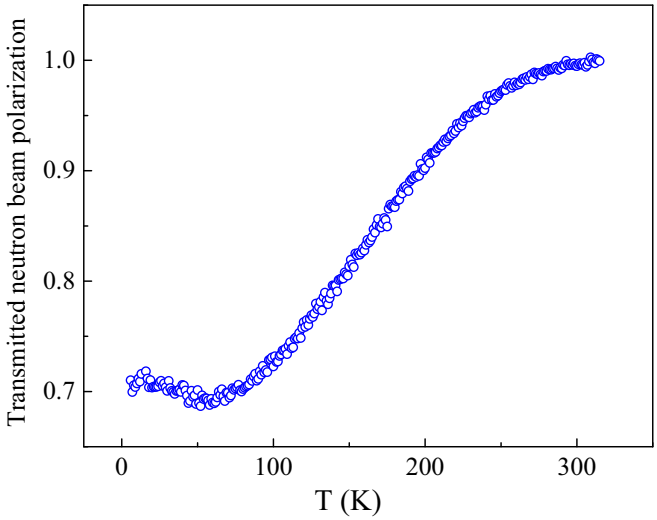

FIG. 10. Temperature dependence of the transmitted neutron polarization under $H = 50$ Oe.

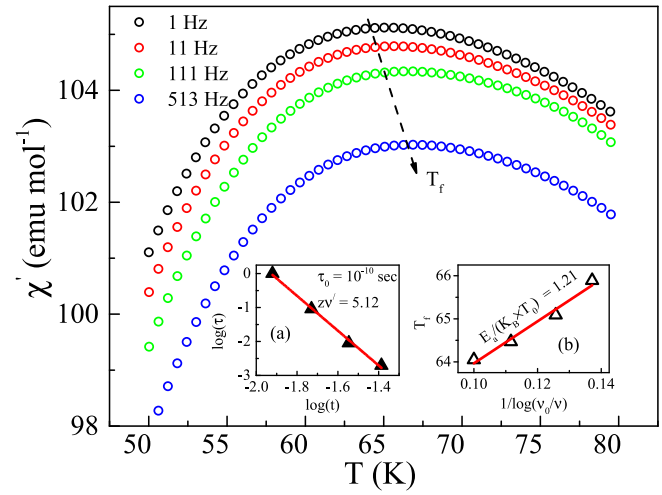

FIG. 11. Temperature dependence of $\chi'(T)$ of NiRuMnSn taken at different frequencies. Inset (a) shows the variation of $\log_{10}(\tau)$ with $\log_{10}(t)$. Inset (b) represents the plot of T_f vs $1/\log_{10}\frac{\nu_0}{\nu}$.

paramagnetic region. As one approaches and moves further below the Curie temperature, the development and subsequent gradual increase of the domain size is reflected in the decreasing trend of the neutron beam polarization signal, as expected in a ferromagnetic material. The polarization signal shows a minimum at ∼60 K, below which the polarization signal starts to grow again. The minimum in polarization around 60 K and increasing nature of polarization for $T < 60$ K can be explained by the decrease in the coherence length of the ferromagnetic interaction due to the decrease in the ferromagnetic domain sizes. The size of the magnetic domains can be estimated using the expression [56,57]

$$P_f = P_i \exp\left[-\alpha\left(\frac{d}{\Delta}\right)\langle\phi_\delta\rangle^2\right], \tag{5}$$

where P_i and P_f are the initial and final transmitted beam polarizations, α is a dimensionless parameter equal to 1/3, d is the sample thickness (which is 7 mm in the studied sample), Δ is the domain size, and the precession angle $\phi_\delta = (4.63 \times 10^{-10}\,\mathrm{G^{-1}\AA^{-2}})\lambda B\Delta$. The domain magnetization B is obtained from the bulk magnetization. The domain size is thus estimated to be 0.2 μm at 5 K. The change in depolarization values below 60 K signifies the reduction in domain sizes, i.e., the enhancement of the number of magnetic spins in the domain boundaries by deviating from the domain magnetization direction. To understand whether this reduction in domain size causes any magnetic phase coexistence, we carried out ac susceptibility measurements.

F. ac susceptibility

Figure 11 represents the temperature variations of the real part of the ac susceptibility χ' performed under low ac field of 5 Oe and different frequencies. $\chi'(T)$ data show a well-rounded peak near 65 K and the frequency dependent character of the peak of $\chi'(T)$ suggests the magnetic anomaly is of spin-glass type. In order to determine the nature of the spin-glass state, i.e., whether it is a canonical or cluster-glass type, we carried out a detailed analysis of the nature of temperature variation of the peak in $\chi'(T)$.

The relative shift in freezing temperature per decade of frequency in a typical glassy system is commonly represented as [59]

$$\delta T_f = \frac{\Delta T_f}{T_f \Delta(\log_{10}\nu)}, \tag{6}$$

where T_f is the freezing temperature and ν is the frequency. The value of δT_f was found to be ∼0.001 for canonical spin glasses [60], ∼0.01 for spin-cluster-glass compounds [12,61–63], and ∼0.1 for numerous known superparamagnetic systems [61]. In the studied compound, δT_f was found to be 0.008, which lies on the border of the canonical spin-glass and cluster-glass regimes. δT_f for a spin-glass state follows the frequency dependence given by [59,64]

$$\tau = \tau_0\left(\frac{T_f - T_{SG}}{T_{SG}}\right)^{-z\nu'}, \tag{7}$$

where τ is the relaxation time associated with the measured frequency ($\tau = 1/\nu$), τ_0 is the single-flip relaxation time, T_{SG} is the spin-glass temperature for $\nu = 0$, and $z\nu'$ is the dynamical critical exponent. The value of $z\nu'$ typically lies between 4 and 12 for the spin-glass state. The value of τ_0 for canonical spin glasses lies in the region of 10^{-13}–10^{-12} s, but for a spin-cluster-glass system it lies mostly in the range of 10^{-11}–10^{-4} s. On the other hand, superparamagnetic states are associated with larger values of τ_0 [61,65]. For NiRuMnSn, the value of $z\nu'$ is found to be 5.1, which is in the range expected for spin-glass state formation, while the estimated $\tau_0 \approx 10^{-10}$ s also lies in the border range of canonical and cluster-glass states.

Another dynamical scaling law, known as the empirical Vogel-Fulcher relation, can be used to simulate spin dynamics in glassy systems around the freezing temperature. The frequency dependence of the freezing temperature can be stated

as [59,66]

$$\nu = \nu_0 \exp\left[-\frac{E_a}{k_B(T_f - T_0)}\right], \tag{8}$$

where ν_0 is known as the characteristic attempt frequency, T_0 is called the Vogel-Fulcher temperature, and E_a is the activation energy. From the T_f vs $1/\log_{10}\frac{\nu_0}{\nu}$ plot for NiRuMnSn, the fitted values are found to be $E_a/K_B \approx 59$ K and $T_0 \approx 48.7$ K. For canonical spin-glass states, the value of $\frac{E_a}{K_B T_0}$ generally comes out to be close to 1, whereas for cluster-glass-type system it assumes a relatively larger value. In the studied compound, the value of $\frac{E_a}{K_B T_0}$ is estimated to be ∼1.21, which is in the canonical spin-glass regime. Combining neutron polarization and ac susceptibility results, it can be said that the domain boundary spin loses its FM nature below 60 K (as discussed in Sec. III E) and is frozen in space, giving rise to the spin-glass state. NiRuMnSn can be viewed as a reentrant spin-glass system where the glassy state formed below the T_C.

IV. CONCLUSION

We synthesized a 4*d*-based quaternary Heusler alloy NiRuMnSn using an arc melting technique. The combined studies utilizing XRD, EXAFS, and neutron diffraction revealed that the compound crystallizes in a partially disordered structure, where Ni and Ru statistically mix in the 4*c* and 4*d* Wyckoff positions. This experimental observation is also supported by the theoretical estimation of lower formation ground-state energy in the disordered structure, containing mixed Ni and Ru atoms in same plane, over the fully ordered one. The compound exhibits a ferromagnetic to paramagnetic transition near 214 K, and the saturation moment at 3 K is estimated to be 2.17 μ_B/f.u., which is much lower than the expected Slater-Pauli value of 5 μ_B/f.u. Neutron diffraction experiments further revealed that the magnetic moment is carried by only the Mn atoms, in agreement with the DFT calculations. Neutron depolarization along with ac susceptibility results confirmed that the gradual growth of the ferromagnetic domains with the lowering of temperature is hindered below 60 K due to the development of a reentrant spin-glass state. A discrepancy between the theoretically estimated moment and the experimentally observed value has been argued to be due to the Ni/Ru site disorder along with the development of a spin-glass phase at low temperature. It is interesting to note that among about a thousand Heusler alloys reported so far, only a handful have been reported to show spin-glass behavior, and thus, NiRuMnSn is a very rare system among the equiatomic quaternary Heusler alloys. Although it is generally believed that isoelectronic substitution of a 3*d* metal with a 4*d* element that has larger atomic radii is likely to improve the structural order and enhance spin polarization in Heusler alloys, our theoretical and experimental results prove that while the structural order indeed improves in NiRuMnSn ($L2_1$ type) in comparison to NiFeMnSn ($D0_3$ type), the nonmagnetic character of isoelectronic Ru (in comparison to Fe) results in a much lower spin-polarization value even in ordered structures.

ACKNOWLEDGMENTS

We would like to thank the late Prof. Vitalij K. Pecharsky, who actively participated in this work and passed away before submission of the paper. S.G. and S.C. would like to sincerely acknowledge SINP, India, and UGC, India, respectively, for their fellowships. DFT calculations were performed using HPC resources from GENCI-CINES (Grant No. 2021-A0100906175). Work at Ames National Laboratory was supported by the Division of Materials Science and Engineering of the Office of Basic Energy Sciences, Office of Science of the U.S. Department of Energy (DOE). Ames National Laboratory is operated for the U.S. DOE by Iowa State University of Science and Technology under Contract No. DE-AC02-07CH11358.

[1] R. A. de Groot, F. M. Mueller, P. G. van Engen, and K. H. J. Buschow, Phys. Rev. Lett. **50**, 2024 (1983).
[2] L. Mañosa, D. González-Alonso, A. Planes, E. Bonnot, M. Barrio, J.-L. Tamarit, S. Aksoy, and M. Acet, Nat. Mater. **9**, 478 (2010).
[3] A. K. Nayak, V. Kumar, T. Ma, P. Werner, E. Pippel, R. Sahoo, F. Damay, U. K. Rößler, C. Felser, and S. S. Parkin, Nature (London) **548**, 561 (2017).
[4] K. Manna, Y. Sun, L. Muechler, J. Kübler, and C. Felser, Nat. Rev. Mater. **3**, 244 (2018).
[5] B. Hinterleitner, I. Knapp, M. Poneder, Y. Shi, H. Müller, G. Eguchi, C. Eisenmenger-Sittner, M. Stöger-Pollach, Y. Kakefuda, N. Kawamoto, Q. Guo, T. Baba, T. Mori, S. Ullah, X.-Q. Chen, and E. Bauer, Nature (London) **576**, 85 (2019).
[6] S. Mondal, C. Mazumdar, R. Ranganathan, E. Alleno, P. C. Sreeparvathy, V. Kanchana, and G. Vaitheeswaran, Phys. Rev. B **98**, 205130 (2018).
[7] J. Liu, T. Gottschall, K. P. Skokov, J. D. Moore, and O. Gutfleisch, Nat. Mater. **11**, 620 (2012).
[8] T. Graf, C. Felser, and S. S. Parkin, Prog. Solid State Chem. **39**, 1 (2011).
[9] N. D. Telling, P. S. Keatley, G. van der Laan, R. J. Hicken, E. Arenholz, Y. Sakuraba, M. Oogane, Y. Ando, K. Takanashi, A. Sakuma, and T. Miyazaki, Phys. Rev. B **78**, 184438 (2008).
[10] J. Barth, G. H. Fecher, B. Balke, S. Ouardi, T. Graf, C. Felser, A. Shkabko, A. Weidenkaff, P. Klaer, H. J. Elmers, H. Yoshikawa, S. Ueda, and K. Kobayashi, Phys. Rev. B **81**, 064404 (2010).
[11] S. Roy, N. Khan, R. Singha, A. Pariari, and P. Mandal, Phys. Rev. B **99**, 214414 (2019).
[12] S. Gupta, S. Chakraborty, S. Pakhira, A. Biswas, Y. Mudryk, A. Kumar, B. Mukherjee, G. S. Okram, A. Das, V. K. Pecharsky, and C. Mazumdar, Phys. Rev. B **107**, 184408 (2023).
[13] C. Felser, G. H. Fecher, and B. Balke, Angew. Chem., Int. Ed. **46**, 668 (2007).
[14] D. Bombor, C. G. F. Blum, O. Volkonskiy, S. Rodan, S. Wurmehl, C. Hess, and B. Büchner, Phys. Rev. Lett. **110**, 066601 (2013).

[15] Y. Miura, K. Nagao, and M. Shirai, Phys. Rev. B **69**, 144413 (2004).

[16] P. Kharel, J. Herran, P. Lukashev, Y. Jin, J. Waybright, S. Gilbert, B. Staten, P. Gray, S. Valloppilly, Y. Huh, and D. J. Sellmyer, AIP Adv. **7**, 056402 (2017).

[17] M. D. Mukadam, S. Roy, S. S. Meena, P. Bhatt, and S. M. Yusuf, Phys. Rev. B **94**, 214423 (2016).

[18] K. Bera, S. Mukherjee, M. Mukadam, S. Mondal, M. Firoz, G. Vaitheeswaran, A. Roy, and S. Yusuf, Appl. Phys. Lett. **121**, 052404 (2022).

[19] L. Bainsla and K. Suresh, Appl. Phys. Rev. **3**, 031101 (2016).

[20] X. Dai, G. Liu, G. H. Fecher, C. Felser, Y. Li, and H. Liu, J. Appl. Phys. **105**, 07E901 (2009).

[21] V. Alijani, S. Ouardi, G. H. Fecher, J. Winterlik, S. S. Naghavi, X. Kozina, G. Stryganyuk, C. Felser, E. Ikenaga, Y. Yamashita, S. Ueda, and K. Kobayashi, Phys. Rev. B **84**, 224416 (2011).

[22] V. Alijani, J. Winterlik, G. H. Fecher, S. S. Naghavi, and C. Felser, Phys. Rev. B **83**, 184428 (2011).

[23] L. Bainsla, A. I. Mallick, M. M. Raja, A. K. Nigam, B. A. D. C. S. Varaprasad, Y. K. Takahashi, A. Alam, K. G. Suresh, and K. Hono, Phys. Rev. B **91**, 104408 (2015).

[24] L. Bainsla, A. I. Mallick, M. M. Raja, A. A. Coelho, A. K. Nigam, D. D. Johnson, A. Alam, and K. G. Suresh, Phys. Rev. B **92**, 045201 (2015).

[25] S. Gupta, S. Chakraborty, S. Pakhira, C. Barreteau, J.-C. Crivello, B. Bandyopadhyay, J. M. Greneche, E. Alleno, and C. Mazumdar, Phys. Rev. B **106**, 115148 (2022).

[26] S. Gupta, S. Chakraborty, V. Bhasin, S. Pakhira, S. Dan, C. Barreteau, J.-C. Crivello, S. Jha, M. Avdeev, J.-M. Greneche, D. Bhattacharyya, E. Alleno, and C. Mazumdar, Phys. Rev. B **108**, 045137 (2023).

[27] S. Gupta, J. Sau, M. Kumar, and C. Mazumdar, arXiv:2303.08589.

[28] D. Rani, Enamullah, K. G. Suresh, A. K. Yadav, S. N. Jha, D. Bhattacharyya, M. R. Varma, and A. Alam, Phys. Rev. B **96**, 184404 (2017).

[29] L. Bainsla, M. M. Raja, A. K. Nigam, and K. G. Suresh, J. Alloys Compd. **651**, 631 (2015).

[30] L. Bainsla, K. Suresh, A. Nigam, M. Manivel Raja, B. C. S. Varaprasad, Y. Takahashi, and K. Hono, J. Appl. Phys. **116**, 203902 (2014).

[31] J. Rodríguez-Carvajal, Phys. B (Amsterdam, Neth.) **192**, 55 (1993).

[32] S. Basu, C. Nayak, A. K. Yadav, A. Agrawal, A. K. Poswal, D. Bhattacharyya, S. N. Jha, and N. K. Sahoo, J. Phys.: Conf. Ser. **493**, 012032 (2014).

[33] A. K. Poswal, A. Agrawal, A. K. Yadav, C. Nayak, S. Basu, S. R. Kane, C. K. Garg, D. Bhattachryya, S. N. Jha, and N. K. Sahoo, in *Solid State Physics: Proceedings of the 58th DAE Solid State Physics Symposium 2013*, AIP Conf. Proc. No. 1591 (AIP, Melville, NY, 2014), pp. 649–651.

[34] D. C. Konigsberger and R. Prins, *X-Ray Absorption: Principles, Applications, Techniques of EXAFS, SEXAFS and XANES* (Wiley, 1988).

[35] B. Ravel and M. Newville, J. Synchrotron Radiat. **12**, 537 (2005).

[36] P. E. Blöchl, Phys. Rev. B **50**, 17953 (1994).

[37] G. Kresse and J. Hafner, Phys. Rev. B **48**, 13115 (1993).

[38] G. Kresse and J. Hafner, J. Phys.: Condens. Matter **6**, 8245 (1994).

[39] J. P. Perdew, K. Burke, and M. Ernzerhof, Phys. Rev. Lett. **77**, 3865 (1996).

[40] P. E. Blöchl, O. Jepsen, and O. K. Andersen, Phys. Rev. B **49**, 16223 (1994).

[41] A. Zunger, S.-H. Wei, L. G. Ferreira, and J. E. Bernard, Phys. Rev. Lett. **65**, 353 (1990).

[42] J. M. Sanchez, F. Ducastelle, and D. Gratias, Phys. A (Amsterdam, Neth.) **128**, 334 (1984).

[43] A. van de Walle, CALPHAD: Comput. Coupling Phase Diagrams Thermochem. **33**, 266 (2009).

[44] A. van de Walle, P. Tiwary, M. De Jong, D. Olmsted, M. Asta, A. Dick, D. Shin, Y. Wang, L.-Q. Chen, and Z.-K. Liu, CALPHAD: Comput. Coupling Phase Diagrams Thermochem. **42**, 13 (2013).

[45] I. Galanakis, P. H. Dederichs, and N. Papanikolaou, Phys. Rev. B **66**, 174429 (2002).

[46] K. Özdoğan, E. Şaşıoğlu, and I. Galanakis, J. Appl. Phys. **113**, 193903 (2013).

[47] P. Webster and K. Ziebeck, J. Phys. Chem. Solids **34**, 1647 (1973).

[48] Y. Venkateswara, D. Rani, K. Suresh, and A. Alam, J. Magn. Magn. Mater. **502**, 166536 (2020).

[49] B. Balke, S. Wurmehl, G. H. Fecher, C. Felser, M. C. Alves, F. Bernardi, and J. Morais, Appl. Phys. Lett. **90**, 172501 (2007).

[50] L. Bainsla, A. Yadav, Y. Venkateswara, S. Jha, D. Bhattacharyya, and K. Suresh, J. Alloys Compd. **651**, 509 (2015).

[51] B. Ravel, M. P. Raphael, V. G. Harris, and Q. Huang, Phys. Rev. B **65**, 184431 (2002).

[52] T. Samanta, P. A. Bhobe, A. Das, A. Kumar, and A. K. Nigam, Phys. Rev. B **97**, 184421 (2018).

[53] J. Kroder, K. Manna, D. Kriegner, A. S. Sukhanov, E. Liu, H. Borrmann, A. Hoser, J. Gooth, W. Schnelle, D. S. Inosov, G. H. Fecher, and C. Felser, Phys. Rev. B **99**, 174410 (2019).

[54] W. Zhang, Y. Sun, H. Wang, Y. Li, X. Zhang, Y. Sui, H. Luo, F. Meng, Z. Qian, and G. Wu, J. Alloys Compd. **589**, 230 (2014).

[55] A. Das, S. Paranjpe, and S. Murayama, Phys. B (Amsterdam, Neth.) **335**, 130 (2003).

[56] A. Das, S. Paranjpe, S. Honda, S. Murayama, and Y. Tsuchiya, J. Phys.: Condens. Matter **11**, 5209 (1999).

[57] O. Halpern and T. Holstein, Phys. Rev. **59**, 960 (1941).

[58] S. Mitsuda, H. Yoshizawa, and Y. Endoh, Phys. Rev. B **45**, 9788 (1992).

[59] J. A. Mydosh, *Spin Glasses: An Experimental Introduction* (CRC Press, Boca Raton, FL, 1993).

[60] B. Mondal, S. Dan, S. Mondal, R. Bhowmik, R. Ranganathan, and C. Mazumdar, Intermetallics **120**, 106740 (2020).

[61] S. Pakhira, C. Mazumdar, R. Ranganathan, S. Giri, and M. Avdeev, Phys. Rev. B **94**, 104414 (2016).

[62] S. Pakhira, C. Mazumdar, R. Ranganathan, and S. Giri, J. Alloys Compd. **742**, 391 (2018).

[63] S. Chakraborty, S. Gupta, S. Pakhira, R. Choudhary, A. Biswas, Y. Mudryk, V. K. Pecharsky, D. D. Johnson, and C. Mazumdar, Phys. Rev. B **106**, 224427 (2022).

[64] T. Mori and H. Mamiya, Phys. Rev. B **68**, 214422 (2003).

[65] J. Lago, S. J. Blundell, A. Eguia, M. Jansen, and T. Rojo, Phys. Rev. B **86**, 064412 (2012).

[66] J. Souletie and J. L. Tholence, Phys. Rev. B **32**, 516 (1985).